Eur. Phys. J. E (2020) **43**: 64
DOI 10.1140/epje/i2020-11985-4

THE EUROPEAN PHYSICAL JOURNAL E

Regular Article

Cracking to curling transition in drying colloidal films

Weipeng Meng[1], Mingchao Liu[1,2], Yixiang Gan[3], Ludovic Pauchard[4], and C.Q. Chen[1,a]

[1] Department of Engineering Mechanics, CNMM & AML, Tsinghua University, Beijing 100084, China
[2] Mathematical Institute, University of Oxford, Oxford, OX2 6GG, UK
[3] School of Civil Engineering, The University of Sydney, Sydney, NSW 2006, Australia
[4] Université Paris-Saclay, CNRS, FAST, 91405, Orsay, France

Received 29 April 2020 / Received in final form 28 August 2020 / Accepted 31 August 2020
Published online: 1 October 2020

Abstract. Drying-induced cracking is widely encountered in nature and is of fundamental interest in industrial applications. During desiccation, the evolution of water content is nonlinear. Considering the inhomogeneous procedure of desiccation, it is worth considering whether water content will affect the crack pattern formation. To address this concern, in this paper, we report an experimental investigation on the effect of water content on the failure mode in drying colloidal films. A distinct failure transition from random cracking to curling is found when the initial water content increases gradually. When the water content is below a critical value for given film thickness, random desiccation cracking driven by shrinkage is observed. Beyond this critical water content, the film curls with the advent of several main cracks. It is also found that the critical water content corresponding to the transition point depends on the film thickness. In order to qualitatively interpret the experimental observation, a theoretical model is established by adopting the fracture mechanics based on the energy method. The model is found to agree well with the experimental results, elucidating the effects of initial water content on the crack patterns and the transition of failure modes.

1 Introduction

From cracks in dried mud to craquelure pattern in old paintings, the formation of cracks due to desiccation of colloidal films is commonly observed. This interesting phenomenon has a long history of both scientific and industrial applications, including the production of industrial and functional coatings [1–3], templates for photonics [4, 5], geophysical phenomena [6,7], and so on. Successful applications rely heavily on the knowledge of the physical processes that determine crack formations. So far, extensive relevant works have been done to improve the understanding of this complex phenomenon [8].

Regarding the desiccation crack of colloidal films, the fundamental mechanisms have been explored and clarified in the past couple of decades. During the drying process, the stress in the films increases, and the films usually fail with cracks on the surface due to the inner stress gradient [9,10]. Three basic failure mechanisms are found for releasing the stress inside the films, including shrinkage cracks perpendicular to the film surface [11–13], delamination of the film from the substrate [14–17], and shear band formation [17–19]. Many works have focused on various effects on shrinkage cracks, *e.g.*, the film thickness [20–23], particle size [9,20,24], properties of the particles [25–27], and substrate properties [21,28–31]. Moreover, the initial water content (*i.e.*, the mass ratio of water to particles) has been found to affect the formation of cracking after desiccation [32]. By considering the stress distribution in the film, quantitative relations between these factors and crack sizes have been obtained.

In addition to patterned cracks, delamination of films is another important failure mode during the drying of colloidal films. However, only a few studies deal with the delamination crack [33,34]. Compared to crack propagation, the delamination of a film is considered to be more complex and difficult, due to additional deformation modes. Also, the factors that affect shrinkage cracks can affect the behavior of film delamination, as reported by Bagchi *et al.* [35]. However, the mechanism has yet to be fully explored. It is important to investigate how the factors affect the failure modes during the drying of colloidal films, in order to understand the nature of the formation of shrinkage cracks and delamination and to facilitate the practical applications of colloidal films.

Here we report an experimental study on the failure mode transition of colloidal films from shrinkage crack to curling from the substrate on account of delamination.

[a] e-mail: chencq@tsinghua.edu.cn

Table 1. Properties of bentonite [36].

Property description	Value	Unit
Specific gravity of soil grain	2.66	/
Liquid limit	276	%
Plastic limit	37	%
Total specific surface area	597	m^2/g
Percent of montmorillonite	75.4	%

The experiments show that the transition can be controlled by varying both the film thickness and the initial water content. The paper is organized as follows: the experimental materials and methods are described in sect. 2. In sect. 3, we show the experimental results and image processing results. The theoretical analysis of the phenomenon is given in sect. 4, with conclusions summarized in sect. 5.

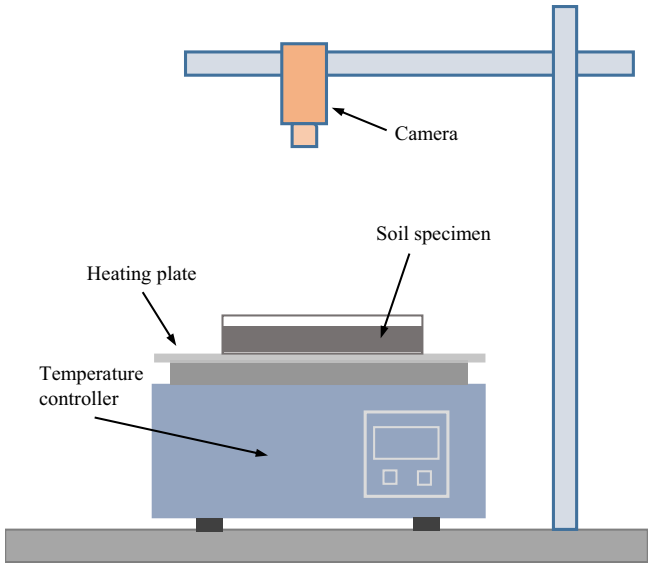

Fig. 1. Schematic diagram of the experimental setup.

2 Materials and methods

2.1 Material properties

The material used in our experiments is sodium bentonite (from Yuanyuan company in Zhengzhou, Henan Province, China). Its major component is montmorillonite, mainly composed of SiO_2 and Al_2O_3 with slight ions of Mg, Ca, Na, and Fe, with the chemical formula of $(Na, Ca)_{0.33}(Al, Mg, Fe)_2[(Si, Al)_4O_{10}](OH)_2 \cdot nH_2O$. The exchangeable cation of bentonite is Na^+. The particle size of the bentonite is slightly dispersed with the average diameter measured by the SEM as $46.1 \pm 4.9\,\mu$m. Properties of the bentonite used in this study are similar to GMZ bentonite which is from GaoMiaoZi deposit in the Inner Mongolia Autonomous Region as given in table 1.

2.2 Experimental methods

Drying experiments of colloidal films with various thicknesses and initial gravimetric water contents are conducted on a heating plate with a constant temperature. A schematic diagram of the experimental setup is shown in fig. 1. The bentonite is dried over rigid circular soda lime silicate glass petri dishes with an internal diameter of 82 mm and a flat and smooth bottom. Initially, the saturated slurry specimens are prepared by mixing bentonite powder and water with different water contents. It is noted that all the mentioned water contents of the present tested specimens in this paper is the water content in mass concentration, unless indicated otherwise. Slurries are then well stirred until smooth and immediately poured evenly into the petri dishes. For all the water contents in our experiments, the slurries behave as fluids (well beyond the liquid limit in table 1), from which we can ignore the memory effect [37–39]. Then, the dishes with bentonite slurries are put on the heating plate with a constant temperature at 40 °C which is maintained throughout the whole experiment. The slurries are dried completely after 6–12 hours, depending on the amount of water in the film. When drying is completed, the bentonite becomes lighter in color, and there are no further cracks. During desiccation, the ambient temperature is about 26 °C, and the relative humidity is $10\% \pm 2\%$. By doing so, the crack patterns of different film thicknesses and water contents can be obtained. To monitor the whole procedure, we put a camera (Sony FDR-AX45) on top of the surface to record the desiccation state of the film.

2.3 Image processing

To describe the crack pattern quantitatively, we use the open-source tool ImageJ to analyze the obtained images. First, we convert the original color images (see fig. 2(a)) to binary images, which means there are only two possible values to show the color in white or black for each pixel. Secondly, we adjust the threshold of the images to clearly show the difference between cracked blocks and cracks. Thirdly, we remove the pixels from the edges of the objects and add pixels to the edge of the objects which are called "erode" and "dilate", respectively, and the small spots of the images are removed. After preprocessing, we get the binary images of the experimental results as shown in fig. 2(b).

Next, we use the software *@ Pore and Crack Analysis System* (PCAS) [40,41] to quantitatively analyze the crack information in the bentonite films in which the failure mode is dominated by cracking. The black and white spots of the images are deleted to reduce the noise (fig. 2(c)). Distribution of crack length, crack width, and crack density can then be calculated (fig. 2(d)). For films failed dominated by curling, we choose the cracked block area density, *i.e.*, the ratio of the projection area of cracked blocks

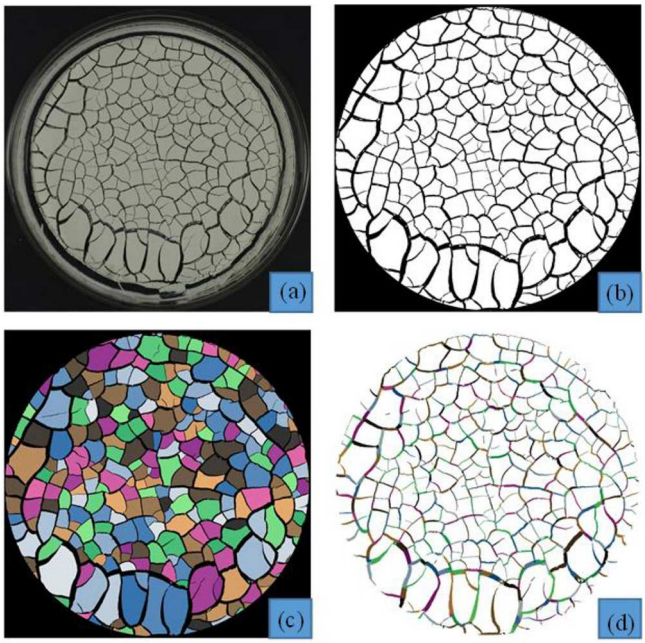

Fig. 2. The procedure of image processing ((a)–(d)): (a) the original image of the experiment, (b) the binary image processed by ImageJ, (c) the cracked blocks analysis of the experiment processed by PCAS, and (d) the crack pattern analysis processed by PCAS. Colors in (c) and (d) are adopted to denote different fracture parts and cracks, respectively.

to the total area of the petri dish, to quantify the extent of curling. Obviously, the cracked blocks area density is smaller if the magnitude of curling gets larger. The image processing results will be discussed in sect. 3.2.

3 Experimental results

3.1 Transition from cracking to curling

In order to investigate the influence of the initial water content on the failure behavior of the bentonite films during drying and how the film thickness affects the final pattern, we conduct a series of experiments with different initial water contents and different thicknesses of the bentonite film (here it is characterized by the dry weight of solid particles, and the relationship between film thickness and film mass will be given in fig. 5). The failure patterns after desiccation are shown in fig. 3. It can be seen that, for a given thickness (*i.e.*, each row in the figure), when the initial water content is lower than a critical value, the films behave normally, and random cracking occurs. For higher intial contents, however, several main cracks can be developed, and subsequently, the film debonds from the substrate and curls to release the strain energy during desiccation. To be more specific, we consider the bentonite film with a mass of 5 g. It can be found that its failure mode transfers from cracking to curling when the initial water content increases (defined as the mass ratio between water and sodium bentonite particles). For the initial water contents of 4.0:1 and 4.5:1, the film cracks randomly to release the energy due to desiccation. When the initial water content reaches 5.0:1, a failure mode transition happens in the film. As a result, not only cracking in the film but also debonding of the film from the substrate is evident. Further increasing the initial water content to 5.5:1 results in more profound curling.

For the range of film thickness reported in this paper, there exists a critical initial water content below which the film cracks randomly to release the strain energy. In the case of films with initial water contents above a critical value, the film debonds from the substrate and curls to release the strain energy. It is noted that increasing the mass of the film favors the cracking mode; as a consequence, the initial water content corresponding to the cracking to curling transition is increased. For instance, a comparison of the failure patterns of the films with a mass of 5 g and 6 g in fig. 3 shows that at the initial water content of 5.0:1, the most favorable failure of the film with 6 g is still cracking while that of the film with 5 g is delamination and curling. Above this initial water content, the film with a mass of 6 g debonds from the substrate and curls to release the energy: the number of cracks decreases. For the initial water content fixed at 5.0:1, the films with the masses of 4 g and 5 g debond from the substrate; the film with a mass of 6 g just shows a transition state that there are some delamination, but the film curls barely; when the mass of the film reaches 7 g, the film cracks normally without delamination. These results show that the initial state of films have an influence on the drying procedure and the final patterns. The paramter of the initial state of the films we considered in this paper is initial water content. It's known to us film desiccation starting from a diluted slur will lead to a thin layer and there will probably be delamination for this thin film if the initial water content is above the critical value. And for the film started with a thin slurry layer of a concentrated solution, the final pattern is random cracking since the initial water content is below the critical value.

To further explore this phenomenon, we measure the evaporation rates during drying in terms of the reduction of total mass as a function of time (see, fig. 4). One can see from fig. 4 that these films with different initial water contents have almost the same evaporation rate. Therefore, the observed features of failure modes in fig. 3 does not depend strongly on the evaporation rate. Also, we conduct experiments with the same thickness and initial water content of films but different temperatures. We find that the films have the same failure mode at 80 °C as that at room temperature. Above 80 °C, the film will also debond from the substrate with a high initial water content. But the cracking pieces of the film are convex ($\cap$) rather than concave ($\cup$).

3.2 Image processing results

As shown in fig. 3, there is a boundary between the two failure modes for colloidal film desiccation with various initial water contents and film thicknesses. First of all, we use SEM to measure the final film thickness given in fig. 5.

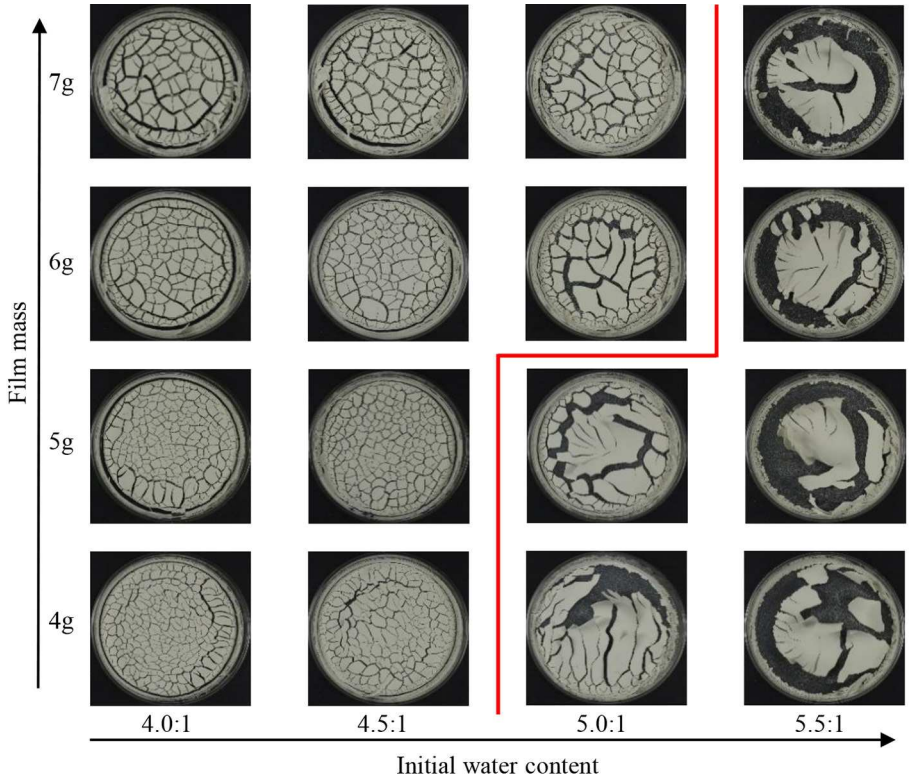

Fig. 3. Diagram showing failure patterns of dried bentonite films as a function of the final film thickness along the vertical axis (the thickness is represented by the mass of the film), and the water contents along the horizontal axis. Drying is performed at 40 °C. The red line shows the transition between two distinct failure modes.

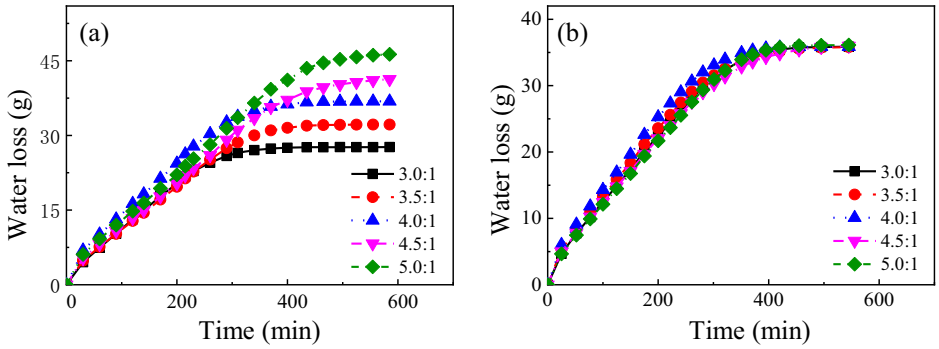

Fig. 4. Measurement of the weight of water loss as a function of time during drying processes. The left figure (a) shows bentonite films with the same thickness, *i.e.*, the same weight of bentonite of 9 g, but different initial water contents. The right figure (b) shows the films with the same initial weight of water of 35 g. By changing the mass of bentonite, we can get different water contents of films. (Here the radius of the petri dish is 110 mm.)

Then, we process the images of cracking mode and curling mode and use different parameters to characterize these two failure modes. To differentiate the cracking and curling modes, we calculate the Euler numbers [42–44] for the observed failure patterns. The results are shown as follows in table 2: the magnitude of the Euler number is large for the cracking mode while it gets smaller with the film thickness increasing or initial water content increasing. One can see that, for the case of initial water content being 5.0:1, there is an abrupt change in the Euler number, corresponding to the phase transition between cracking mode and curling mode as the film thickness decreases.

For the cracking mode, we consider the effects of the crack area density (*i.e.*, defined as the area ratio of crack to the whole substrate), crack length, and crack width to quantify the cracking patterns, as shown in fig. 6. Figure 6(a) shows how the crack area density changes if the film fails according to the cracking failure mode. We know that high initial water content can lead to the failure mode changing from cracking to curling. As for the initial water contents of 4.0:1 and 4.5:1, the film still has a stable cracking failure mode and the crack area density has an upward tendency with the film thickness increasing. For the initial water content of 5.0:1, the film's failure mode

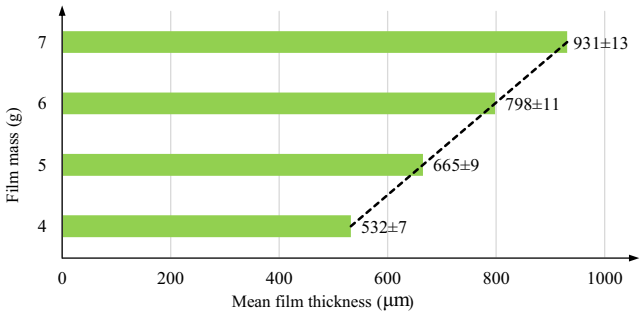

Fig. 5. Mean film thickness of desiccation films corresponding to the film mass measured by the SEM.

Table 2. The Euler number of experimental results.

Film thickness (μm)	Initial water content			
	4.0:1	4.5:1	5.0:1	5.5:1
931	−193	−147	−143	−5
798	−213	−188	−149	−12
665	−286	−236	−87	−4
532	−292	−252	−47	−8

is cracking with the thicknesses of 798 μm and 931 μm. The transition boundary of the failure mode from cracking to curling lies at the initial water content of 5.0:1 for films with a thickness of 665 μm. As for the thicknesses of 532 μm and 665 μm, the film delaminates from the substrate, which will be discussed later. In the line of initial water content equal to 5.0:1, there exists a transition of the failure mode from curling to cracking with the film thickness increasing. It is known that increasing film thickness would inhibit the curling mode. Obviously, if the film debonded from the substrate, the projected crack area density should be bigger than that of the cracking mode. This is why the crack area density of the film with a thickness of 798 μm is bigger than that of the film with a thickness of 931 μm.

The statistics of crack numbers are shown in fig. 6(b). From this figure we can see that the bentonite film with the initial water contents of 4.0:1 and 4.5:1 has a stable regular crack pattern and the crack number has a downward tendency with the film thickness increasing. The failure mode of the film with an initial water content of 5.0:1 has a tendency to curl with the film thickness decreasing. For the curling mode, there are less cracks and the increase of film thickness has an inhibition to curling tendency, which makes that there are not many changes between the film thicknesses of 798 μm and 931 μm with an initial water content of 5.0:1.

Moreover, we also get the total crack length and average crack width, as shown in figs. 6(c) and (d), sharing the same feature as discussed above. For the initial water contents of 4.0:1 and 4.5:1, the film has a stable regular crack pattern. As the film thickness increases, the total crack length decreases and the average crack width increases. For the initial water content of 5.0:1, there exists a mode transition from curling to cracking with increasing film thickness. For the influence of curling tendency, there are only small changes in the total crack length and average crack width between the film thickness of 798 μm and 931 μm with an initial water content of 5.5:1.

For the film with the failure mode of curling, we use the film area density (*i.e.*, defined as the projection area ratio of film to the whole substrate) to present the magnitude of curling displayed in fig. 7. This figure shows that the film area density is more sensitive to the change in the initial water content than the one in the film thickness, at least within the range considered here. It should be noted that uncertainty is expected in the measuring of film area density when the curling film region cracks due to the gravity force of the upper curling part.

4 Theoretical analysis

In this section, a theoretical model is presented to explain the failure mode transition (from cracking to curling) observed in the experiments. It is assumed that the cracking and curling each has a critical stress at which the film cracks or curls. The transition is the result of the competition of these two critical stresses. Note that the strain energy in the film due to desiccation releases when the film cracks or debonds from the substrate. According to Griffith's theory [45], new surfaces are created upon cracking and the energy needed for creating the new surfaces is from the energy stored in the film. For the case of the film debonding from the substrate, it is assumed that the way to release the strain energy is to create new surfaces between the film and substrate and the film curls to further minimize the stored strain energy. For the cracking and debonding having different critical stresses, the failure of film is controlled by the stress in the film. Both the initial water content and the film thickness have an influence on the transition between the two failure modes in the experimental results, which means that the critical stresses associated with the two failure modes have a relationship with the two factors. Detailed discussion is shown in the section below.

For random cracking of bentonite films, Tirumkudulu and Russel [9] obtained the critical stress

$$\frac{\sigma_c}{2\gamma/R} = 0.187\left(\frac{2R}{h}\right)^{2/3}\left(\frac{GM_0R\phi_{rcp}}{2\gamma}\right)^{1/3}, \qquad (1)$$

where R is the particle radius, G is the shear modulus of the particles, γ is the surface energy per unit area corresponds to the interfacial energy between water and air, h is the film thickness, M_0 is the number of contacting neighbors, and ϕ_{rcp} is the random close-packing concentration. If the stress in the film reaches the critical stress σ_c, random cracks can be formed in the films.

Similarly, a critical stress corresponding to film delamination exists. To determine the critical stress of debonding, we have to know the driving energy of the film and the debonding energy. Using the beam bonding to a substrate

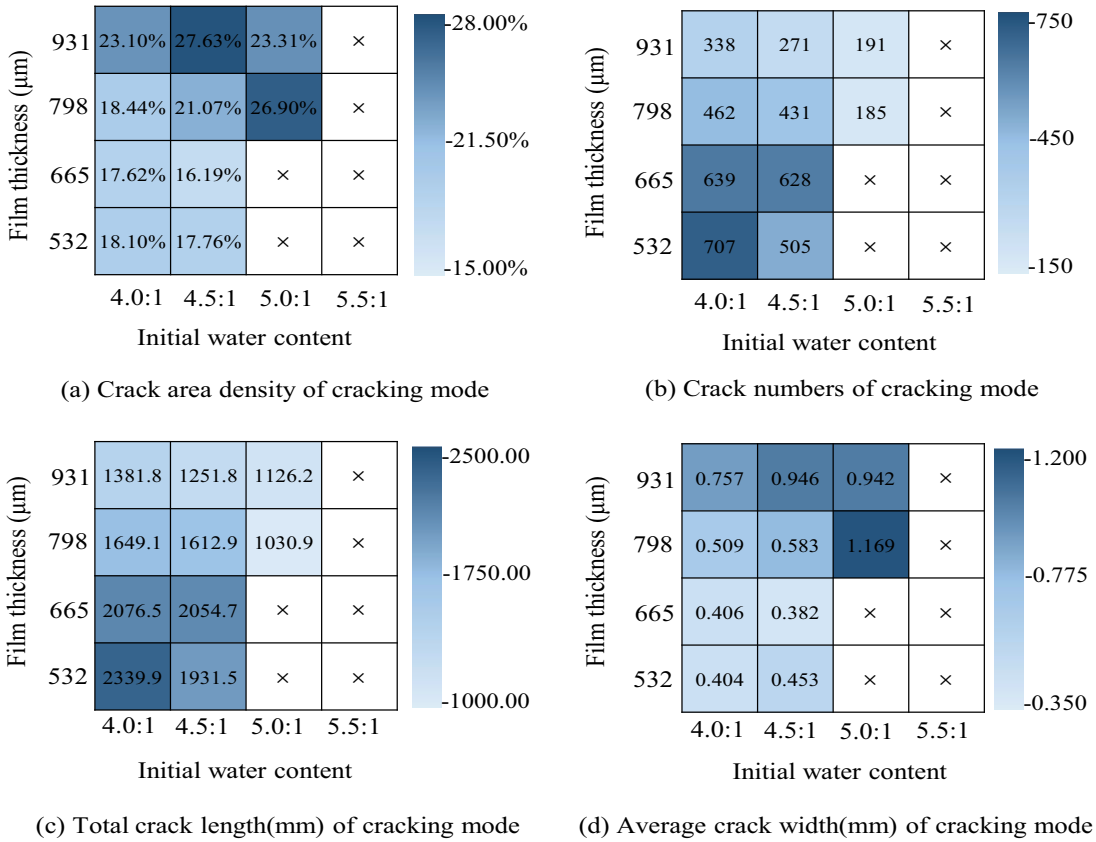

(a) Crack area density of cracking mode

(b) Crack numbers of cracking mode

(c) Total crack length(mm) of cracking mode

(d) Average crack width(mm) of cracking mode

Fig. 6. Crack properties of the cracking failure mode.

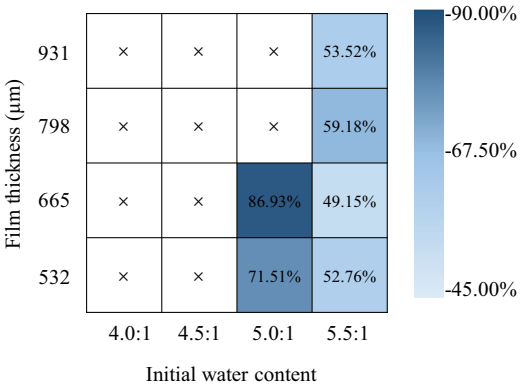

Fig. 7. Film area density of the curling failure mode.

model, Hutchinson and Suo [46] proposed the energy release rate of debonding to be

$$G_{ss} = \frac{1}{2E}\left(\frac{P^2}{h} + 12\frac{M^2}{h^3}\right), \tag{2}$$

where E is Young's modulus, P is the axial force, h is the beam thickness, and the bending moment M is related to the difference of the forces P^+ and P^- on the top and bottom surfaces of the film by

$$M \propto \left(P^+ - P^-\right)\frac{h}{2}. \tag{3}$$

From the experimental results of Kitsunezaki [47], the level of the pore pressure is around 100 kPa when the crack happens and the difference of the pore pressure is about 100 Pa at most. Therefore, a first-order approximation of the forces P^+ and P^- is $P^+ - P^- \approx 10^{-3}P$. We can then estimate the second term on the right-hand side of eq. (2) to be around

$$\frac{M^2}{h^3} \approx \frac{10^{-6}}{4}\frac{P^2}{h}, \tag{4}$$

which is negligible compared to the force term in eq. (2). Accordingly, we can simplify the energy release rate as

$$G_{ss} \approx \frac{1}{2E}\frac{P^2}{h} \approx \frac{1}{2E}\frac{(\sigma_0 h)^2}{h} = \frac{1}{2E}\sigma_0^2 h. \tag{5}$$

The delamination criterion of the film from the substrate is

$$G_{ss} = \Gamma_i, \tag{6}$$

where Γ_i is the surface energy needed for delamination. The corresponding critical stress for debonding is then given by

$$\sigma_0 = \sqrt{\frac{2E\Gamma_i}{h}}. \tag{7}$$

It is noted that for the colloidal film bonded to a substrate considered in this paper, the surface energy for debonding Γ_i can be calculated as follows. In accordance with

Smith *et al.* [21], it can be assumed that the bentonite particles involved with debonding are those initially absorbed on the substrate at the beginning of desiccation and the particles are spherical. Consider the total number of the particles in the film being N, and the average radius of the particle being R_0. The volume of the particles is $V_0 = 4N\pi R_0^3/3$. After mixing the particles with water, an equivalent radius of the particle R_1 can be introduced to be

$$\frac{4\pi N R_1^3}{3} = V_1 \tag{8}$$

where V_1 is the sum of the volumes of water and bentonite. Moreover, R_1 depends upon R_0 and the initial water content φ_0 via

$$\frac{R_1}{R_0} = \left(\frac{V_1}{V_0}\right)^{1/3} = \left(\frac{\rho_w + \varphi_0\rho_p}{\rho_w}\right)^{1/3}, \tag{9}$$

where ρ_p is the density of the bentonite particle and ρ_w is the density of the water. With the equivalent particle radius, we can get the number of the particles bonding to the substrate as

$$n = \frac{A}{\pi R_1^2}, \tag{10}$$

where A is the bottom surface area of the substrate. Neglecting the interaction between particles, the total bonding energy per unit area of the film to the substrate is the sum of that for individual particles, *i.e.*,

$$\Gamma_i = \frac{n\Gamma_p}{A}, \tag{11}$$

with Γ_p being the bonding energy per particle. Combing eqs. (9)–(11) yields

$$\Gamma_i = \frac{\Gamma_p}{\pi R_0^2}\left(\frac{\rho_p}{\rho_w}\right)^{-2/3}\varphi_0^{-2/3}. \tag{12}$$

According to eq. (7), the critical stress for film delamination is then given by

$$\sigma_d = \sqrt{\frac{2E\Gamma_i}{h}} = \frac{1}{R_0}\sqrt{\frac{2E\Gamma_p}{\pi h}}\left(\frac{\rho_p}{\rho_w}\right)^{-1/3}\varphi_0^{-1/3}. \tag{13}$$

Figure 3 shows the two competing failure modes of the film, *i.e.*, cracking and curling following film desiccation. According to eqs. (1) and (13), cracking prevails if $\sigma_c < \sigma_d$. Otherwise, curling becomes the dominant failure mode. Therefore, the transition condition from cracking to curling can be obtained by setting $\sigma_c = \sigma_d$, that is

$$h = 8.55 \times 10^{-5}\frac{\pi^3 R_0^6\gamma^4\left(GM_0\phi_{rcp}\right)^2}{E^3\Gamma_p^3}\left(\frac{\rho_p}{\rho_w}\right)^2\varphi_0^2 \tag{14}$$

where the particle radius R_0 is 23.1 μm, the shear modulus G is 135 MPa, the surface energy γ is 0.072 N/m, the number of contacting neighbors M_0 is 6, and the random close-packing concentration ϕ_{rcp} is 0.6. In fact, an accurate measurement of the binding energy per particle Γ_p, combining inter-particle forces resulting from capillary bridges, van der Waals, and electrostatic forces, is formidable. Although we can simplify Γ_p to be the capillary bridges between particles and the substrate, it is still very hard to get the accurate current water content. Nevertheless, it can be inferred from the measured failure diagram plotted in the initial water content-film thickness space, as shown in fig. 8, where red and green symbols denote the observed cracking and curling modes, respectively.

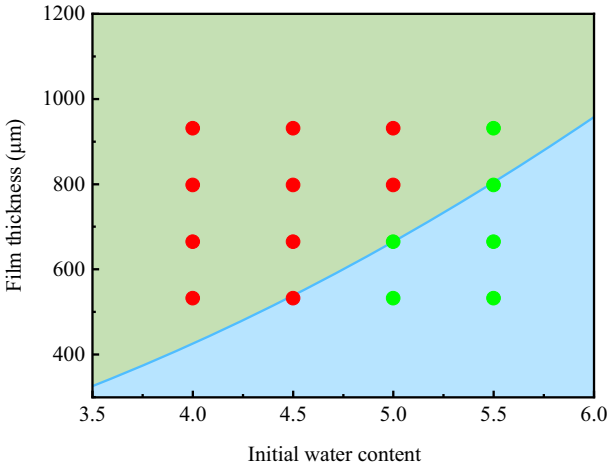

Fig. 8. Phase diagram of the failure mode of the drying colloidal films. The red circular dots in the figure indicate the state of typical cracking films after desiccation and the green dots mean that the films not only crack but also debond from the substrate. The blue line shows the theoretical prediction of the failure mode transition of the film. Below the blue line, it is energetically more favorable for the film to debond from the substrate.

From fig. 8, we can see that two regions corresponding to cracking and curling are present and a boundary between them exists. As a rule of thumb, the state of initial water content of 5.0:1 and film thickness of 665 μm can be deemed to be on the boundary. Because the boundary is actually governed by the transition (eq. (14)), we can then extract $\Gamma_p = 2.49 \times 10^{-13}$ J from eq. (14) with $\varphi_0 = 5$ and $h = 665\,\mu$m. The cracking-to-curling transition condition eq. (14) is plotted in fig. 8 as a solid line and is shown to be able to capture the overall trend of the experimental results. However, we do see a deviation between the predictions and experiments. For instance, failure at the point with initial water content being 5.5:1 and film thickness of 931 μm is predicted to be cracking while curling is observed. Such a discrepancy may be due to the simplifications adopted in our theoretical model. For instance, the particles are assumed to be spherical and uniformly sized, and the bending moment in the film is negligible. Nevertheless, the obtained failure transition model not only serves as a guidance to differentiate cracking and curling, but it also provides a qualitative tool to estimate the binding energy per particle of the colloidal film.

5 Conclusions

Drying of colloidal films can be affected by many factors, including the properties of the solute and solvent, the

influence of film thickness, and the amount of solute. The effect of this last parameter has yet to be fully explored. Here we report that the amount of solvent composing a colloidal film impacts the final desiccation morphology of the film. Experiments show that the colloidal films exhibit two ways to release the strain energy during desiccation, due to the changes of the amount of solvent and the film thickness. For a fixed film thickness, there is a transition for the film from cracking to debonding with increasing amount of water. This phenomenon shows the importance of the solvent and gives a reference for the study of solvent effects. To explain this phenomenon, we assume that the number of particles attached to the substrate on the bottom of the film remains the same as that at the beginning of desiccation immediately before delamination. We use the energy balancing model for this phenomenon. The obtained theory can explain the results well. Experimental results, with the support of the proposed theoretical model, elucidate the role of the solvent amount in the crack patterns as well as the transition of failure modes.

This work is supported by the National Natural Science Foundation of China (Nos. 11732007 and 11921002) and the Science Challenge Project of China (Grant No. TZ2018007). ML acknowledges the support of a Newton International Fellowship from the Royal Society. YG acknowledges the support from The University of Sydney SOAR Fellowship and the Australian Research Council Discovery Project DP170104192.

Author contribution statement

Weipeng Meng: methodology, software, formal analysis, data curation, writing —original draft. Mingchao Liu: conceptualization, investigation, visualization, writing —review and editing, funding acquisition. Yixiang Gan: validation, writing —review and editing, funding acquisition. Ludovic Pauchard: writing —review and editing. C.Q. Chen: resources, writing —review and editing, supervision, project administration, funding acquisition.

References

1. Y. Ma, H.T. Davis, L.E. Scriven, Prog. Org. Coat. **52**, 46 (2005).
2. R. Gupta, K.D.M. Rao, K. Srivastava, A. Kumar, S. Kiruthika, G.U. Kulkarni, ACS Appl. Mater. Interfaces **6**, 13688 (2014).
3. J.H. Prosser, T. Brugarolas, S. Lee, A.J. Nolte, D. Lee, Nano Lett. **12**, 5287 (2012).
4. F. Juillerat, P. Bowen, H. Hofmann, Langmuir **22**, 2249 (2006).
5. J. Zhang, Z. Sun, B. Yang, Curr. Opin. Colloid Interface Sci. **14**, 103 (2009).
6. L. Goehring, R. Conroy, A. Akhter, W.J. Clegg, A.F. Routh, Soft Matter **6**, 3562 (2010).
7. L. Goehring, Philos. Trans. R. Soc. Math. Phys. Eng. Sci. **371**, 20120353 (2013).
8. L. Goehring, A. Nakahara, T. Dutta, S. Kitsunezaki, S. Tarafdar, *Desiccation Cracks and Their Patterns: Formation and Modelling in Science and Nature* (Wiley-VCH Verlag GmbH & Co. KGaA, Weinheim, Germany, 2015).
9. M.S. Tirumkudulu, W.B. Russel, Langmuir **21**, 4938 (2005).
10. W.P. Lee, A.F. Routh, Langmuir **20**, 9885 (2004).
11. K.A. Shorlin, J.R. de Bruyn, M. Graham, S.W. Morris, Phys. Rev. E **61**, 6950 (2000).
12. H. Colina, S. Roux, Eur. Phys. J. E **1**, 189 (2000).
13. C.-S. Tang, B. Shi, C. Liu, W.-B. Suo, L. Gao, Appl. Clay Sci. **52**, 69 (2011).
14. L. Pauchard, Europhys. Lett. **74**, 188 (2006).
15. F. Giorgiutti-Dauphiné, L. Pauchard, Colloids Surf. Physicochem. Eng. Asp. **466**, 203 (2015).
16. F. Giorgiutti-Dauphiné, L. Pauchard, Soft Matter **11**, 1397 (2015).
17. B. Yang, J.S. Sharp, M.I. Smith, Sci. Rep. **6**, 32296 (2016).
18. P.-C. Kiatkirakajorn, L. Goehring, Phys. Rev. Lett. **115**, 088302 (2015).
19. B. Yang, J.S. Sharp, M.I. Smith, ACS Nano **9**, 4077 (2015).
20. H.N. Yow, M. Goikoetxea, L. Goehring, A.F. Routh, J. Colloid Interface Sci. **352**, 542 (2010).
21. M.I. Smith, J.S. Sharp, Langmuir **27**, 8009 (2011).
22. V. Lazarus, L. Pauchard, Soft Matter **7**, 2552 (2011).
23. T. Khatun, T. Dutta, S. Tarafdar, Eur. Phys. J. E **38**, 83 (2015).
24. M.S. Tirumkudulu, W.B. Russel, Langmuir **20**, 2947 (2004).
25. L. Pauchard, B. Abou, K. Sekimoto, Langmuir **25**, 6672 (2009).
26. V.R. Dugyala, H. Lama, D.K. Satapathy, M.G. Basavaraj, Sci. Rep. **6**, 30708 (2016).
27. S. Koga, S. Inasawa, Colloids Surf. Physicochem. Eng. Asp. **563**, 95 (2019).
28. K.F. DeCarlo, N. Shokri, Water Resour. Res. **50**, 3039 (2014).
29. U.U. Ghosh, M. Chakraborty, A.B. Bhandari, S. Chakraborty, S. DasGupta, Langmuir **31**, 6001 (2015).
30. Y. Chen, A. Askounis, V. Koutsos, P. Valluri, Y. Takata, S.K. Wilson, K. Sefiane, Langmuir **36**, 204 (2020).
31. T. Liu, H. Luo, J. Ma, W. Xie, Y. Wang, G. Jing, Eur. Phys. J. E **39**, 24 (2016).
32. N. Mohammad, W. Meng, Y. Zhang, M. Liu, A. El-Zein, Y. Gan, Environ. Geotech. (2020) `https://doi.org/10.1680/jenge.19.00112`.
33. K.M. Tran, H.H. Bui, J. Kodikara, M. Sánchez, Can. Geotech. J. **57**, 408 (2020).
34. B. Sobac, P. Colinet, L. Pauchard, Soft Matter **15**, 2381 (2019).
35. A. Bagchi, G.E. Lucas, Z. Suo, A.G. Evans, J. Mater. Res. **9**, 1734 (1994).
36. Z. Wen, Chin. J. Rock Mech. Eng. **25**, 794 (2006).
37. A. Nakahara, Y. Matsuo, J. Phys. Soc. Jpn. **74**, 1362 (2005).
38. Y. Matsuo, A. Nakahara, J. Phys. Soc. Jpn. **81**, 024801 (2012).
39. H. Nakayama, Y. Matsuo, O. Takeshi, A. Nakahara, Eur. Phys. J. E **36**, 1 (2013).

40. C. Liu, B. Shi, J. Zhou, C. Tang, Appl. Clay Sci. **54**, 97 (2011).
41. C. Liu, C.-S. Tang, B. Shi, W.-B. Suo, Comput. Geosci. **57**, 77 (2013).
42. H.-J. Vogel, H. Hoffmann, A. Leopold, K. Roth, Geoderma **125**, 213 (2005).
43. T. Khatun, T. Dutta, S. Tarafdar, Eur. Phys. J. E **38**, 83 (2015).
44. S. Dutta, S. Sen, T. Khatun, T. Dutta, S. Tarafdar, Front. Phys. **7**, 61 (2019).
45. A.A. Griffith, Philos. Trans. R. Soc. London A **221**, 163 (1921).
46. Z. Suo, J.W. Hutchinson, Int. J. Fract. **43**, 1 (1990).
47. S. Kitsunezaki, J. Phys. Soc. Jpn. **78**, 064801 (2009).